

# Processing of Very High Resolution Spaceborne Sliding Spotlight SAR Data Using Velocity Scaling

Yuan Wu, Guang-Cai Sun, *Member, IEEE*, Chun Yang, Jun Yang, Mengdao Xing, *Member, IEEE*, and Zheng Bao, *Senior Member, IEEE*

**Abstract**—In spaceborne synthetic aperture radar, the sliding spotlight mode can acquire high resolution and large azimuth scene size simultaneously. However, when the resolution is very high and the azimuth scene size is large, the traditional hyperbolic range model (HRM) is inaccurate and the variation of the equivalent velocity in azimuth dimension cannot be ignored. Thus, the traditional imaging algorithms based on HRM are no longer available. For this problem, this paper proposes an equivalent acceleration range model, which can precisely take into account the spaceborne curved orbit. Then, velocity scaling algorithm based on this new range model is proposed to meet the needs of very high resolution and large azimuth scene size. The results of the simulation validate the effectiveness of the new range model and the imaging algorithm.

**Index Terms**—Large azimuth scene size, sliding spotlight SAR, synthetic aperture radar (SAR), very high resolution.

## I. INTRODUCTION

IN SPACEBORNE synthetic aperture radar (SAR), high resolution and wide swath are two important aspects in development. New imaging modes and imaging algorithms arose continuously to achieve higher resolution and wider swath [1]–[6]. The sliding spotlight mode [7], [8] can achieve higher resolution than the stripmap mode and larger azimuth scene size than the staring spotlight mode by the steering of the antenna. In the case of very high resolution and large azimuth scene size, as the complexity of spaceborne geometry, the curved orbit cannot be taken into account precisely by the hyperbolic range model (HRM) [1]. The azimuth variation of the equivalent velocity should be considered properly. Thus, the traditional imaging algorithms based on HRM are not valid any more.

In [9], an imaging algorithm for ultrahigh-resolution spaceborne sliding spotlight SAR on curved orbit was proposed,

which considered the azimuth variation of the equivalent velocity and divided the entire data into subapertures. HRM was assumed in each subaperture. However, there needs to be a matching procedure in subaperture recombination, as each subaperture has different model parameters. In [10], a modified equivalent squint range model (MESRM) was developed by introducing the equivalent radar acceleration into the range model in a way different from this paper. Then, a high-order imaging algorithm was derived. However, this modified range model does not consider the azimuth variation of the equivalent velocity. In [11], the author treated the difference between linear track approximation and real curved orbit as a motion error to compensate. However, the compensation was computed for a reference target in the middle of the scene so that it is accurate when the azimuth scene size is small. The accuracy will deteriorate when the azimuth scene size is large.

This paper proposes an equivalent acceleration range model (EARM), which can precisely take into account the spaceborne curved orbit geometry in the case of very high resolution and large azimuth scene size. Based on this range model, this paper proposes the velocity scaling algorithm (VSA), which can process very high resolution spaceborne sliding spotlight SAR data effectively.

This paper is organized as follows. Section II analyzes the azimuth variation of the equivalent velocity and its influence on imaging. In addition, a new EARM is proposed with the precision analysis in this section. Then, Section III gives the VSA with detailed procedures and block diagram. Section IV presents the results of simulation to validate the effectiveness of the new range model and the imaging algorithm. Conclusions are drawn in Section V.

## II. EARM

### A. Range Model

In spaceborne SAR, the satellite moves around the Earth, whereas the Earth is rotating itself from west to east. When the satellite moves to different latitudes, the ground tangential velocity changes accordingly. When the resolution is low, the spaceborne curved orbit can be taken into account by HRM; only the actual velocity is replaced with a virtual velocity called the equivalent velocity. HRM can be expressed as

$$R_{\text{hyp}}(t_a) = \sqrt{r^2 + (v_r(t_a - t_0))^2} \quad (1)$$

Manuscript received April 11, 2015; revised June 12, 2015 and August 22, 2015; accepted September 18, 2015. Date of publication October 26, 2015; date of current version February 24, 2016. This work was supported by the National Natural Science Foundation of China under Grant 61301292.

Y. Wu, G.-C. Sun, J. Yang, M. Xing, and Z. Bao are with the National Laboratory of Radar Signal Processing, Xidian University, Xi'an 710071, China (e-mail: rsands@126.com).

C. Yang is with the Institute of Electronics, Chinese Academy of Sciences, Beijing 100080, China.

Color versions of one or more of the figures in this paper are available online at <http://ieeexplore.ieee.org>.

Digital Object Identifier 10.1109/TGRS.2015.2481923

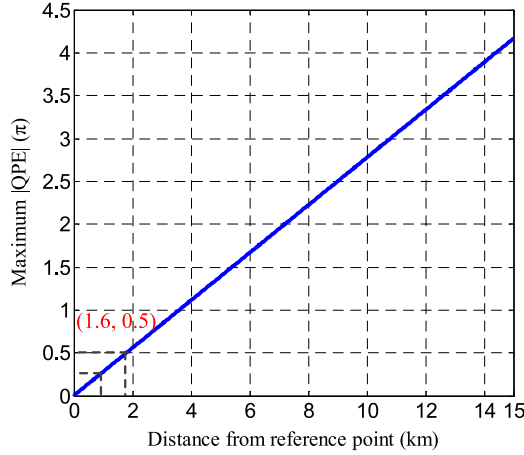


Fig. 1. Maximum  $|QPE|$  due to the azimuth variation of the equivalent velocity, corresponding to 0.15-m azimuth resolution.

where  $t_a$  is the slow time,  $r$  is the range vector of the closest approach distance,  $t_0$  is the zero-Doppler time of the point target, and  $v_r$  represents the equivalent velocity. In [11], the authors analyzed the approximation error of HRM and the azimuth variation of the equivalent velocity in the case of very high resolution, which leads to two conclusions: 1) the approximation error of HRM is huge enough to cause serious azimuth defocusing; and 2) the azimuth variation of the equivalent velocity also has influence on azimuth focusing. The influence of the azimuth variation can be evaluated by quadratic phase error (QPE) [11], i.e.,

$$\varphi(f_a) = -\frac{4\pi}{\lambda} r \left( \sqrt{1 - \left( \frac{\lambda f_a}{2v_r} \right)^2} - \sqrt{1 - \left( \frac{\lambda f_a}{2v_{r,\text{ref}}} \right)^2} \right) \quad (2)$$

where  $f_a$  is the azimuth frequency,  $\lambda$  is the wavelength, and  $v_{r,\text{ref}}$  represents the equivalent velocity of the reference target. The target far from the reference target in azimuth dimension causes large QPE value. When the azimuth bandwidth is large, the QPE value cannot be neglected. Fig. 1 shows the maximum  $|QPE|$  at the edge of the azimuth spectrum, which corresponds to 0.15-m azimuth resolution. The reference target is located at  $-105^\circ/45^\circ$  (longitude/latitude). The analyzed targets are located at different azimuth positions with different equivalent velocities but at the same slant range. The satellite orbit parameters are shown in Table I. If not specified, the satellite orbit parameters shown in Table I are the default configuration. As we can see, the maximum  $|QPE|$  exceeds  $\pi/4$  when the distance from the reference point is 0.8 km and exceeds  $\pi/2$  when the distance is 1.6 km. Thus, in the case of very high resolution and large azimuth scene size, the azimuth variation of the equivalent velocity will be a problem that must be solved.

In [11], the authors treated the difference between the linear track approximation and the real curved orbit as a motion error to compensate. In the other words, the motion compensation range model (MCRM) can be expressed as

$$R_{\text{mot}}(t_a) = \sqrt{r^2 + (v_r(t_a - t_0))^2} + \delta r_{\text{hyp}}(t_a) \quad (3)$$

TABLE I  
SATELLITE ORBIT PARAMETERS

Height	514 km
Eccentricity	0.0011
Inclination	$97.44^\circ$
Semi-major axis	6885 km
Argument of perigee	$97.44^\circ$
Ascending node	$260^\circ$
Incidence angle	$34.8^\circ$

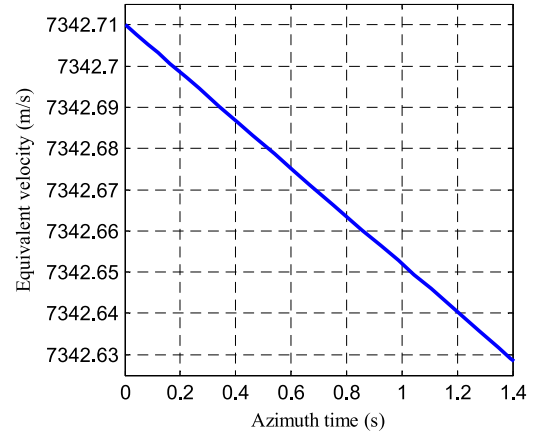


Fig. 2. Variation of the equivalent velocity in azimuth dimension.

where  $\delta r_{\text{hyp}}(t_a)$  is the motion error computed for a reference target in the middle of the scene. The compensation is accurate for the reference target. However, the accuracy deteriorates when the azimuth scene size is large.

On researching of the satellite orbits of different latitudes and different incidence angles, it can be found that the equivalent velocity is changing mildly along azimuth direction, which can be represented by a straight line, except that the slope of the line is affected by the latitude and incidence angle slightly. Fig. 2 shows the variation of the equivalent velocity in azimuth dimension during 1.4 s. The satellite is moving from south to north at latitude of  $45^\circ$ . The incidence angle is  $34.8^\circ$ , and the eccentricity is 0.0011. If we think of the satellite as moving along a straight line with a constant acceleration, as indicated in Fig. 3, we can get  $v_{r,t_0} = v_{r,\text{ref}} + a_r(t_0 - t_{\text{ref}})$ , where  $a_r$  represents the equivalent acceleration,  $t_{\text{ref}}$  is the reference azimuth time constant, which can be set to 0 for convenience, and  $v_{r,\text{ref}}$  represents the equivalent velocity at the reference azimuth time. By integrating  $v_{r,t_0} = v_{r,\text{ref}} + a_r(t_0 - t_{\text{ref}})$  from  $t_0$  to  $t_a$ , we can get a new range model as in (4), shown at the bottom of the page. When  $a_r = 0$ , (4) degenerates to the HRM. It is thus clear that (4) has the ability to take into account the azimuth variation of the equivalent velocity, which makes it more complete and universal.

Even (4) can take into account the azimuth variation of the equivalent velocity, and it is more complete than the HRM, it has high-order terms residual compared with the actual range history, because the satellite is moving along a curved orbit, instead of a straight line orbit shown in Fig. 3. The fourth-order range model (FORM4) proposed in [12] approximates the spaceborne SAR range history very well in the case of very

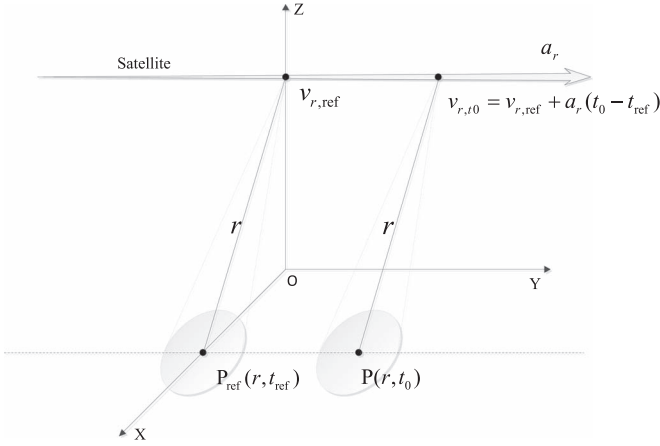


Fig. 3. Equivalent acceleration range model.

high resolution and small azimuth scene size. We use FORM4 to derive the EARM. The FORM4 equation can be written as

$$R_{4th}(t_a) = r + c_1(t_a - t_0) + c_2(t_a - t_0)^2 + c_3(t_a - t_0)^3 + c_4(t_a - t_0)^4 \quad (5)$$

where  $c_1$ ,  $c_2$ ,  $c_3$ , and  $c_4$  represent the coefficients of the first-, second-, third-, and fourth-order terms, respectively. Fig. 4 shows the approximation error of FORM4, which corresponds to 0.15-m azimuth resolution and 8.4-s synthetic aperture time. The reference target is located at  $-105^\circ/45^\circ$  (longitude/latitude). The actual range history for criterion is obtained by professional satellite orbit simulation software. It can be seen that FORM4 has high precision at very high resolution.

Compute the Taylor series of (4) and ignore the higher than fourth-order terms, i.e.,

$$\hat{R}(t_a) = r + \frac{v_{r,t0}^2}{2r}(t_a - t_0)^2 + \frac{a_r v_{r,t0}}{2r}(t_a - t_0)^3 + \left( \frac{a_r^2}{8r} - \frac{v_{r,t0}^4}{8r^3} \right) (t_a - t_0)^4. \quad (6)$$

Because  $t_0$  is the zero-Doppler time of the point target, the linear term is neglected in (5). Let  $c_2 = v_{r,t0}^2/2r$ , then the difference of (5) and (6) can be computed as

$$\Delta R(t_a) = R_{4th}(t_a) - \hat{R}(t_a) = \left( c_3 - \frac{a_r v_{r,t0}}{2r} \right) (t_a - t_0)^3 + \left( c_4 - \frac{a_r^2}{8r} + \frac{v_{r,t0}^4}{8r^3} \right) (t_a - t_0)^4. \quad (7)$$

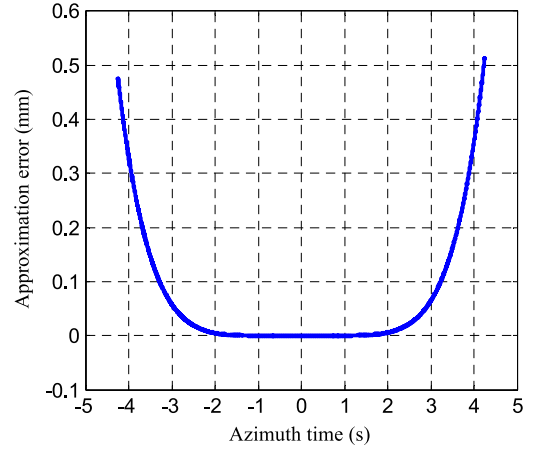


Fig. 4. Approximation error of FORM4, corresponding to 0.15-m azimuth resolution.

Thus, the actual range history can be expressed as (4) plus (7), i.e., (8), shown at the bottom of the page, where  $\beta = c_3 - (a_r v_{r,t0}/2r)$ , and  $\gamma = c_4 - (a_r^2/8r) + (v_{r,t0}^4/8r^3)$ , which are the third- and fourth-order residual coefficients, respectively.  $\beta$  and  $\gamma$  can be assumed constant for they have very little variation in the scene. Finally, the EARM is obtained.

The main parameters of the EARM are the reference equivalent velocity  $v_{r,ref}$ , the equivalent acceleration  $a_r$ , the third-order coefficient  $\beta$ , and the fourth-order coefficient  $\gamma$ .  $a_r$  can be computed from the slope of the varying equivalent velocity in azimuth dimension.  $\beta$  and  $\gamma$  can be computed from the range history of the central target:  $\beta = c_3 - (a_{rS} v_{rS,ref}/2r_S)$  and  $\gamma = c_4 - (a_{rS}^2/8r_S) + (v_{rS,ref}^4/8r_S^3)$ , where  $r_S$ ,  $v_{rS,ref}$ , and  $a_{rS}$  are the slant range, the equivalent velocity, and the equivalent acceleration of the central target, respectively.

### B. Range Model Precision Analysis

Four targets are selected to analyze the precision of HRM, MCRM, MESRM, and EARM. The central target is located at  $-105^\circ/45^\circ$  (longitude/latitude). The other three targets are located 5, 10, and 15 km away from the central target, respectively, in azimuth dimension, but at the same slant range. Fig. 5 shows the phase errors of four range models at four targets, which correspond to 0.15-m azimuth resolution and 8.4-s synthetic aperture time. The actual range history for criterion is obtained by professional satellite orbit simulation software.

$$\hat{R}(t_a) = \sqrt{r^2 + \left( \left( v_{r,ref} t_a + \frac{1}{2} a_r (t_a - t_{ref})^2 \right)^2 - \left( v_{r,ref} t_0 + \frac{1}{2} a_r (t_0 - t_{ref})^2 \right)^2 \right)} \quad (4)$$

$$R(t_a) = \sqrt{r^2 + \left( \left( v_{r,ref} t_a + \frac{1}{2} a_r (t_a - t_{ref})^2 \right)^2 - \left( v_{r,ref} t_0 + \frac{1}{2} a_r (t_0 - t_{ref})^2 \right)^2 \right)} + \beta (t_a - t_0)^3 + \gamma (t_a - t_0)^4 \quad (8)$$

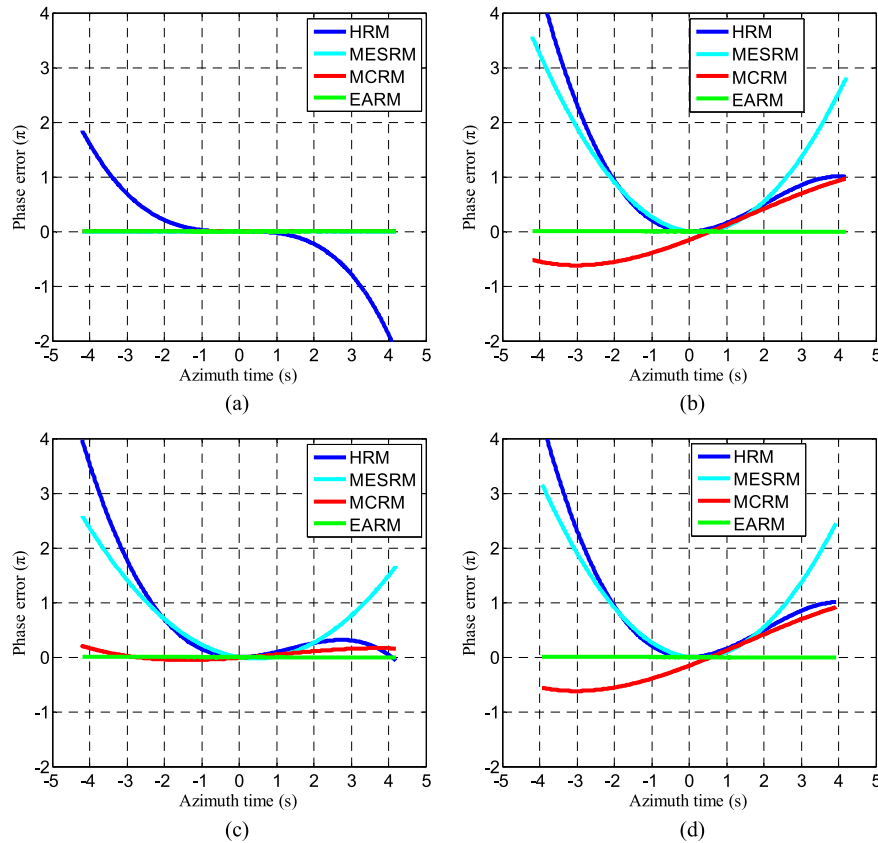


Fig. 5. Phase errors of four range models corresponding to 0.15-m azimuth resolution. (a) Phase errors at the central target. (b) Phase errors at the target 5 km away. (c) Phase errors at the target 10 km away. (d) Phase errors at the target 15 km away.

It can be seen that HRM produces significant error at all four targets. MESRM and MCRM are accurate at the central target, but they are less accurate at the farther targets. EARM is accurate at all four targets, which proves that it can precisely take into account the spaceborne curved orbit.

Three matched filters are applied on the aforementioned four targets to compress the azimuth signals, which are constructed with the MESRM, MCRM, and EARM models, respectively. The impulse responses are shown in Fig. 6, which correspond to 0.15-m azimuth resolution and 8.4-s synthetic aperture time. The axis scales in the left column are different from those in the other columns. It should be noted that the analysis here does not consider the rotation of the radar beam in the sliding spotlight mode. As we can see, the matched filter constructed with MESRM focuses well at the central target. However, the focusing result deteriorates rapidly as the distance from the central target increases, which illustrates that the MESRM model cannot adapt to the azimuth variation of the range history. The matched filter constructed with MCRM focuses well at the central target, too. As the distance from the central target increases, the focusing result deteriorates mildly, which illustrates that the MCRM model can adapt to the azimuth variation of range history in some level, but when the azimuth scene size is large, it is less accurate. The matched filter constructed with EARM focuses well at all four targets, which illustrates that the EARM model can adapt to the azimuth

variation of range history and meet the needs of very high resolution and large azimuth scene size.

To show the azimuth imaging performances of MESRM, MCRM, and EARM at different azimuth positions, the simulations are performed, respectively. The peak sidelobe ratio (PSLR), integrated sidelobe ratio (ISLR), and impulse response width (IRW) results are shown in Fig. 7, which correspond to 0.15-m azimuth resolution and 8.4-s synthetic aperture time. The measured values are plotted without curve smoothing in Fig. 7 and the following figures here. As we can see, the MESRM model is suitable for very small azimuth scene size. The MCRM model can adapt to small azimuth scene size. When the azimuth scene size is large, it will lead to the deterioration of the imaging performance, particularly the PSLR level. The EARM model shows stable imaging performance when the azimuth scene is large.

The preceding analysis corresponds to 0.15-m azimuth resolution without windowing the azimuth filter. To show the azimuth imaging performances of MESRM, MCRM, and EARM as a function of azimuth resolution, simulations are performed on the aforementioned four targets. The results are shown in Fig. 8. As we can see, all three models can achieve very high azimuth resolution at the central target. The MCRM model can achieve higher resolution than MESRM at the other three targets. The EARM model can achieve higher resolution than MCRM at the other three targets.

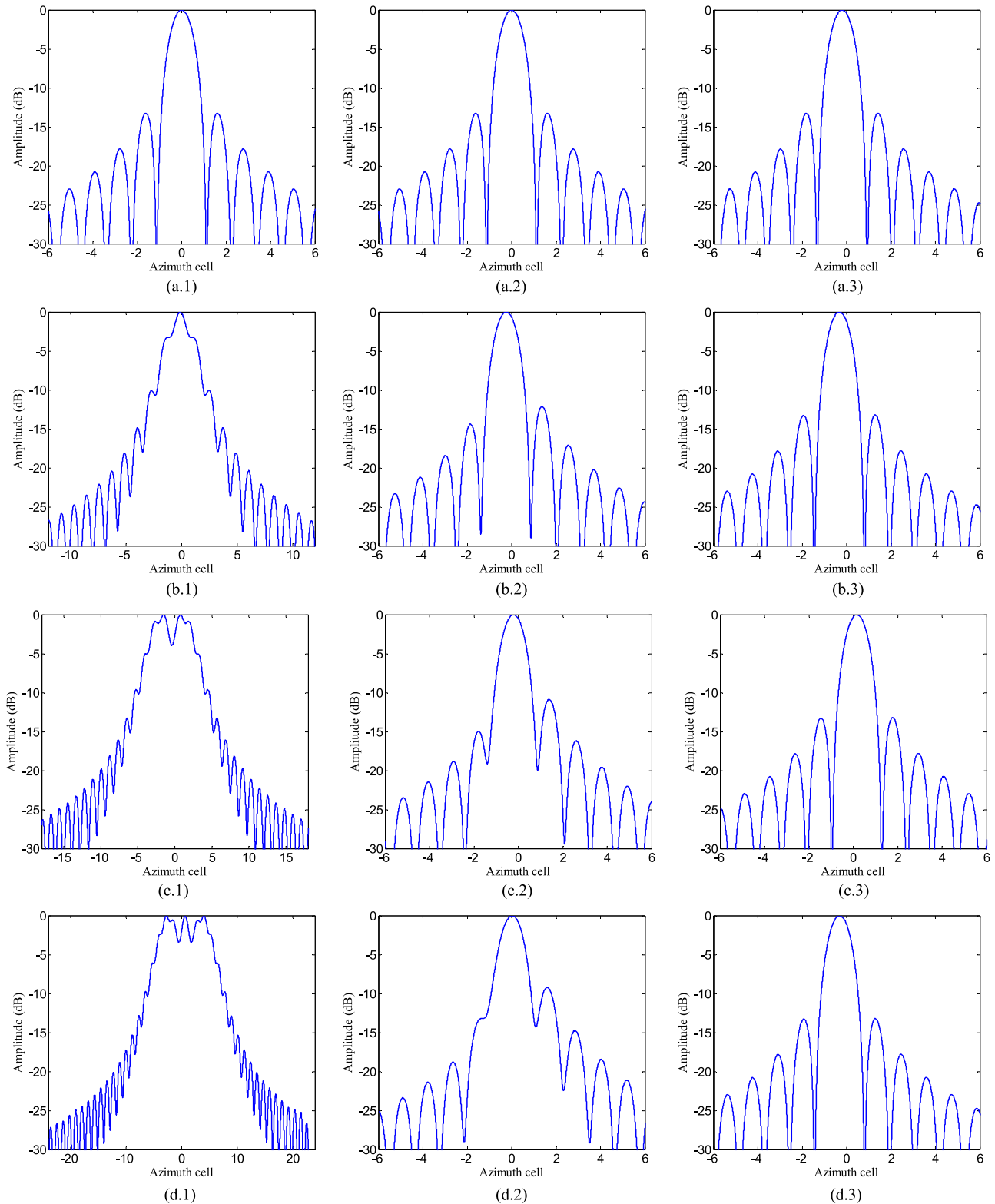


Fig. 6. Impulse responses of matched filters constructed with MESRM, MCRM, and EARM corresponding to 0.15-m azimuth resolution. (a) Results at the central target. (b) Results at the target 5 km away. (c) Results at the target 10 km away. (d) Results at the target 15 km away. (Left column) Results of matched filters constructed with MESRM. (Middle column) Results of matched filters constructed with MCRM. (Right column) Results of matched filters constructed with EARM. The axis scales of the left column are different from the other columns.

The latitude is fixed to  $45^\circ$  in the preceding analysis. There are a few latitudes where the velocity variation in azimuth direction is not dominantly linear, it is quadratic instead.

The EARM model performs well even under these latitudes, because the velocity variation is so small under these latitudes that a linear velocity approximation is accurate enough. Two

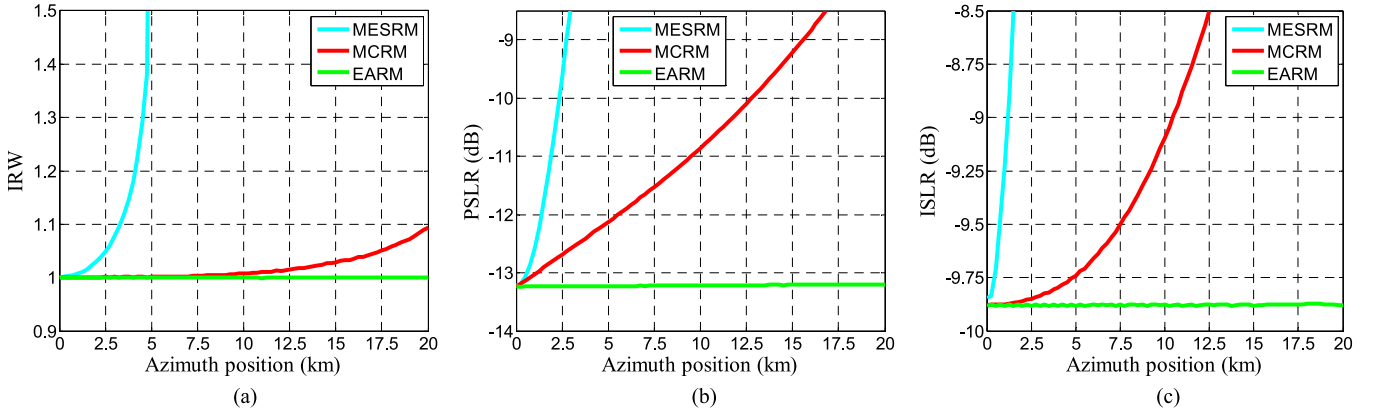


Fig. 7. Azimuth imaging performances of MESRM, MCRM, and EARM at different azimuth positions corresponding to 0.15-m azimuth resolution. (a) IRW of the three models at different azimuth positions. (b) PSLR of the three models at different azimuth positions. (c) ISLR of the three models at different azimuth positions.

targets are selected under latitudes of  $0^\circ$ ,  $22.5^\circ$ ,  $67.5^\circ$ , and  $90^\circ$ , respectively. The first target is the central target for reference. The second target is located 10 km away from the central target in azimuth dimension but at the same slant range. Fig. 9 shows the phase errors of MESRM, MCRM, and EARM at the second target under four latitudes, which correspond to 0.15-m azimuth resolution and 8.4-s synthetic aperture time. It can be observed that the EARM model performs well in different latitudes. Under latitude of  $90^\circ$ , the equivalent velocity variation is quadratic. Using a nearly zero equivalent acceleration, the phase error of the EARM model is very small.

To sum up, the preceding analysis leads to the conclusion that the EARM model can meet the needs of very high resolution and large azimuth scene size and it is better than MESRM and MCRM in this case.

### III. IMAGING ALGORITHM

The VSA based on the EARM is proposed here, which can be decomposed to four steps, as shown in Fig. 10. The first step is the subapertures division, which is used to remove the azimuth aliasing in sliding spotlight SAR. The second step is velocity scaling, which is used to remove the azimuth variation of the equivalent velocity through azimuth time resampling. The third step is the removal of third- and fourth-order residuals, which is implemented in 2-D frequency domain uniformly. The last step is range cell migration correction (RCMC) and azimuth focusing to get final SAR image, where RCMC is realized by an improved  $\omega - k$  algorithm [13], and the azimuth focusing is realized by baseband azimuth scaling (BAS) [7]. Details of the proposed algorithm are provided in the following.

#### A. Subapertures Division

In the sliding spotlight mode, the total azimuth bandwidth is much greater than the pulse repetition frequency (PRF). Two methods are usually adopted to solve the azimuth aliasing

problem, namely, the two-step processing method [14] and the subaperture method [7], which is adopted here. First, the whole data are divided into several subapertures. In the sliding spotlight mode, the radar beam is pointing to a fixed virtual rotation center during the moving of the satellite; thus, each subaperture has a different Doppler centroid frequency, and the data should be transformed to the azimuth baseband first in some procedures in the following.

#### B. Velocity Scaling

Linear FM signals are transmitted from the radar. Echo signal after demodulation can be expressed as

$$S_{\text{sub}}(\hat{t}, t_a) = W_r\left(\hat{t} - \frac{2R(t_a)}{c}\right) \exp\left(j\pi\gamma\left(\hat{t} - \frac{2R(t_a)}{c}\right)^2\right) \times W_a(t_a - t_0) \exp\left(-j\frac{4\pi}{\lambda}R(t_a)\right) \quad (9)$$

where  $R(t_a)$  represents the EARM model (8),  $W_r(\cdot)$  is the window function of linear FM signal,  $W_a(\cdot)$  is the window function in azimuth,  $\hat{t}$  is the fast time,  $c$  is the propagation velocity of light, and  $\gamma$  is the chirp rate of the transmitted signal.

After a range fast Fourier transform (FFT) and range compression by

$$H_1 = \exp\left(j\pi\frac{f_r^2}{\gamma}\right) \quad (10)$$

we get

$$S_{\text{sub}}(f_r, t_a) = W_r(f_r)W_a(t_a - t_0) \exp\left(-j\frac{4\pi}{c}(f_c + f_r)R(t_a)\right) \quad (11)$$

where  $f_r$  is the range frequency. As discussed in Section II, the EARM is based on the assumption that the satellite is moving with a constant acceleration. Thus, if we make an azimuth time



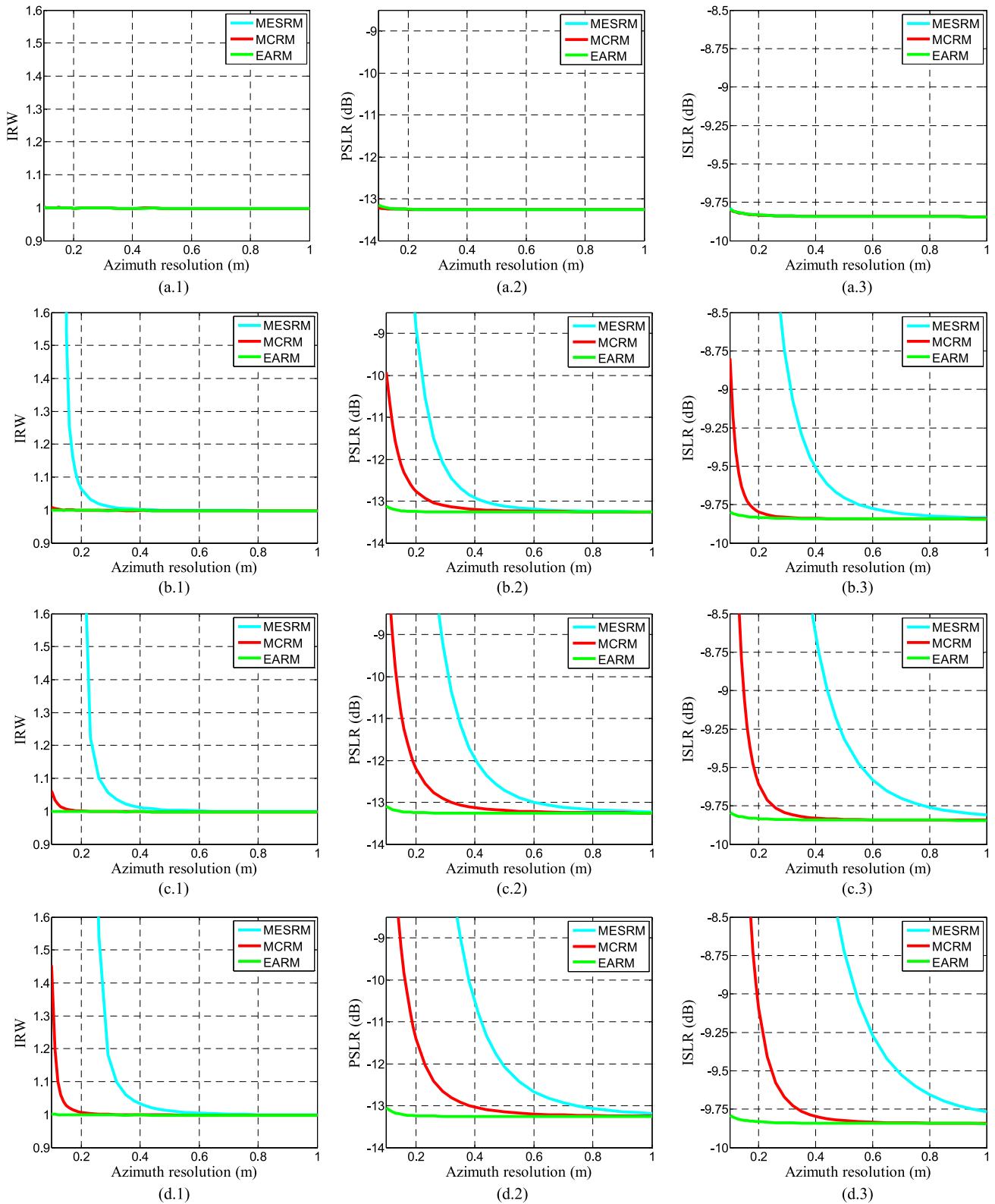


Fig. 8. Azimuth imaging performances of MESRM, MCRM, and EARM as a function of azimuth resolution. (a) Performances at the central target. (b) Performances at the target 5 km away. (c) Performances at the target 10 km away. (d) Performances at the target 15 km away. (Left column) IRW of the three models. (Middle column) PSLR of the three models. (Right column) ISLR of the three models.

scaling according to the moving rule of the satellite, increase the azimuth time interval when the satellite is faster and decrease

the azimuth time interval when the satellite is slower, then the satellite can be thought moving with a constant equivalent

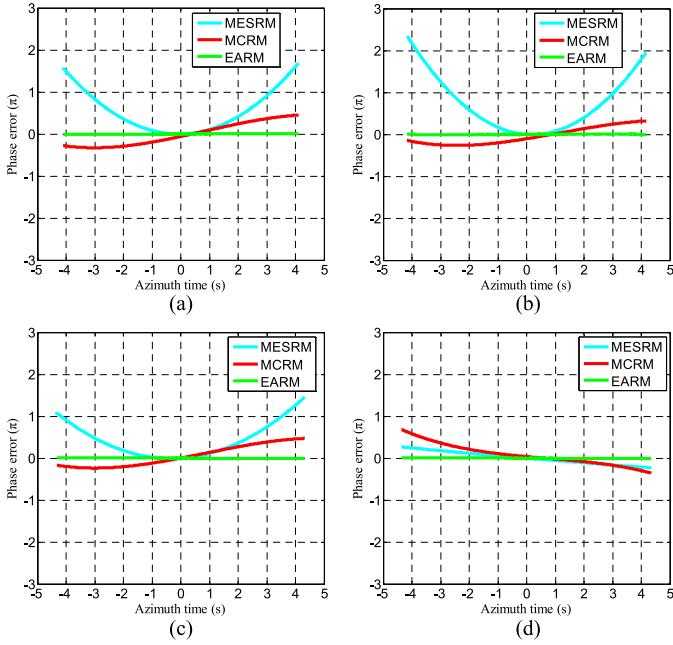


Fig. 9. Phase errors of MESRM, MCRM, and EARM at the second target under different latitudes corresponding to 0.15-m azimuth resolution. (a) Phase errors under latitude of  $0^\circ$ . (b) Phase errors under latitude of  $22.5^\circ$ . (c) Phase errors under latitude of  $67.5^\circ$ . (d) Phase errors under latitude of  $90^\circ$ .

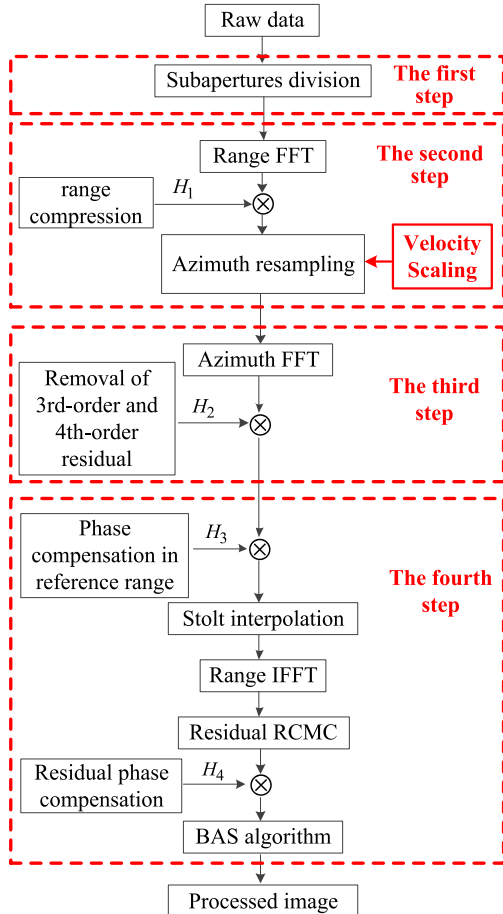


Fig. 10. Block diagram of the proposed algorithm.

velocity in the new azimuth time domain. Thus, if we resample the signal in azimuth time domain according to

$$t_a' = t_a + \sigma_r(t_a - t_{\text{ref}})^2 \quad (12)$$

where  $\sigma_r = (1/2)(a_r/v_{r,\text{ref}})$  is the resampling factor, in the new azimuth time domain  $t_a'$ , the range history can be expressed as

$$\begin{aligned} R(t_a') &= \sqrt{r^2 + (v_{r,\text{ref}}(t_a' - t_0'))^2} \\ &+ \beta \left( \frac{2(t_a' - t_0')}{\sqrt{1 + 4\sigma_r(t_a' - t_{\text{ref}})} + \sqrt{1 + 4\sigma_r(t_0' - t_{\text{ref}})}} \right)^3 \\ &+ \gamma \left( \frac{2(t_a' - t_0')}{\sqrt{1 + 4\sigma_r(t_a' - t_{\text{ref}})} + \sqrt{1 + 4\sigma_r(t_0' - t_{\text{ref}})}} \right)^4 \\ &\approx \sqrt{r^2 + (v_{r,\text{ref}}(t_a' - t_0'))^2} + \beta(t_a' - t_0')^3 + \gamma(t_a' - t_0')^4 \end{aligned} \quad (13)$$

where  $t_0' = t_0 + \sigma_r(t_0 - t_{\text{ref}})^2$ . The definitions of  $\beta$  and  $\gamma$  can be seen in (8). It can be seen that the radical sign term in (13) is the traditional HRM model, which illustrates that the equivalent velocity is azimuth invariant now.

The equivalent acceleration  $a_r$  is almost invariant in the whole imaging scene, so is the resampling factor  $\sigma_r$ . Thus, we can resample the whole signal according to  $\sigma_{rS} = (1/2)(a_{rS}/v_{rS,\text{ref}})$ , which is the resampling factor of the scene center. Then we can get the signal

$$\begin{aligned} S_{\text{sub}}(f_r, t_a') &= W_r(f_r)W_a(t_a' - t_0') \exp \left( -j \frac{4\pi}{c} (f_c + f_r) R(t_a') \right) \end{aligned} \quad (14)$$

where  $R(t_a')$  is expressed by (13). For convenience,  $t_a'$ ,  $t_0'$ , and  $v_{r,\text{ref}}$  are replaced with  $t_a$ ,  $t_0$ , and  $v_r$ , respectively, in the following statement.

In the procedure of resampling, normal sinc interpolation core  $h(t_a) = \text{sinc}(t_a)$  cannot be used, due to the fact that the azimuth frequency of the subaperture may exceed  $(-PRF/2, PRF/2)$ . In order to interpolate correctly, the central frequency of sinc interpolation core should be transformed to  $f_{dc}$ , which is the Doppler centroid frequency of the subaperture. The new established sinc interpolation core is

$$h_{\text{new}}(t_a) = \text{sinc}(t_a) \cdot \exp(j2\pi f_{dc} t_a). \quad (15)$$

After velocity scaling, the equivalent velocity is azimuth invariant now. The third- and fourth-order residuals will be removed in the next step. Since the recombination of subapertures has to be done later, the azimuth resampling in each subaperture should be performed according to (12) uniformly, and the sampling interval in the new azimuth time domain after resampling should be the same as that before resampling in



all subapertures. Thus, the new azimuth time samples in each subaperture coincide with each other and can be recombined easily. The velocity scaling in this part is realized by an interpolation in azimuth. This is a relatively accurate method with little approximation based on the EARM model. To enhance the efficiency of the imaging algorithm, the nonlinear azimuth scaling [15] using a high-order phase term multiplication in azimuth time domain is an optional approach to do the same thing as the azimuth interpolation.

### C. Removal of Third- and Fourth-Order Residuals

According to the stationary phase principle [16], transform the signal expressed by (14) to 2-D frequency domain, i.e.,

$$S_{\text{sub}}(f_r, f_a) = A_0 W_r(f_r) W_a(f_a) \times \exp\left(-j4\pi r \sqrt{\left(\frac{f_c + f_r}{c}\right)^2 - \left(\frac{f_a + f_{dc}}{2v_r}\right)^2}\right) \times \exp(j\varphi_{3;r}) \exp(j\varphi_{4;r}) \exp(-j2\pi(f_a + f_{dc})t_0) \quad (16a)$$

$$\varphi_{3;r} = \pi\beta \frac{r^3(f_c + f_r)(f_a + f_{dc})^3}{2cv_r^6} \times \left(\sqrt{\left(\frac{f_c + f_r}{c}\right)^2 - \left(\frac{f_a + f_{dc}}{2v_r}\right)^2}\right)^{-3} \quad (16b)$$

$$\varphi_{4;r} = -\pi\gamma \frac{r^4(f_c + f_r)(f_a + f_{dc})^4}{4cv_r^8} \times \left(\sqrt{\left(\frac{f_c + f_r}{c}\right)^2 - \left(\frac{f_a + f_{dc}}{2v_r}\right)^2}\right)^{-4} \quad (16c)$$

where  $A_0$  is a constant which has no influence on imaging, and  $f_a$  is the azimuth frequency. During the derivation of (16a)–(16c), the third- and fourth-order terms are ignored to solve the stationary point.  $\varphi_{3;r}$  and  $\varphi_{4;r}$  have little variation over range dimension, so compensate the phase caused by the third- and fourth-order residuals using

$$H_2 = \exp(-j\varphi_{3;r}) \exp(-j\varphi_{4;r})|_{r=r_S}. \quad (17)$$

Then the signal can be expressed as

$$S_{\text{sub}}(f_r, f_a) = A_0 W_r(f_r) W_a(f_a) \times \exp\left(-j4\pi r \sqrt{\left(\frac{f_c + f_r}{c}\right)^2 - \left(\frac{f_a + f_{dc}}{2v_r}\right)^2}\right) \times \exp(-j2\pi(f_a + f_{dc})t_0). \quad (18)$$

So far, the third- and fourth-order residuals have been removed, so does the azimuth variation of the equivalent velocity. The form of the signal is the same as that of the traditional HRM model. However, the range variation of the equivalent velocity still exists. The RCMC and the azimuth focusing will be done in the next step.

### D. RCMC and Azimuth Focusing

Some algorithms developed for SAR data processing can be found in [17]–[20]. The  $\omega - k$  algorithm is selected to perform the RCMC due to its accuracy and polychromatic property. However, the original  $\omega - k$  algorithm cannot deal with the range variation of the equivalent velocity. A modified  $\omega - k$  algorithm was mentioned in [11], where the author did not give the detailed processing, which is discussed in the following.

Compensate the nonlinear phase of the signal in the reference range  $r_S$  with

$$H_3(f_r, f_a) = \exp\left(-j4\pi r_S \sqrt{\left(\frac{f_c + f_r}{c}\right)^2 - \left(\frac{f_a + f_{dc}}{2v_{rS}}\right)^2}\right) \quad (19)$$

where  $v_{rS}$  is the equivalent velocity at the reference slant range. The phase of the signal in the range  $r \neq r_S$  has not been completely compensated, leaving a residual phase

$$\varphi_{\text{resi}} = -4\pi(r - r_S) \sqrt{\left(\frac{f_c + f_r}{c}\right)^2 - \left(\frac{f_a + f_{dc}}{2v_{rS}}\right)^2} - 4\pi r \left(\sqrt{\left(\frac{f_c + f_r}{c}\right)^2 - \left(\frac{f_a + f_{dc}}{2v_r}\right)^2} - \sqrt{\left(\frac{f_c + f_r}{c}\right)^2 - \left(\frac{f_a + f_{dc}}{2v_{rS}}\right)^2}\right). \quad (20)$$

Then Stolt interpolation is done according to

$$f_r' = \sqrt{(f_c + f_r)^2 - \left(\frac{c(f_a + f_{dc})}{2v_{rS}}\right)^2} - f_c. \quad (21)$$

Substituting the preceding equation into (20), we can get

$$\varphi_{\text{resi}} = -4\pi(r - r_S) \frac{f_c + f_r'}{c} - 4\pi r \left(\sqrt{\left(\frac{f_c + f_r'}{c}\right)^2 + \left(\frac{f_a + f_{dc}}{2v_{rS}}\right)^2} - \left(\frac{f_a + f_{dc}}{2v_r}\right)^2 - \frac{f_c + f_r'}{c}\right). \quad (22)$$

The Taylor series of (22) is

$$\varphi_{\text{resi}}(f_r') = \phi_0 + \phi_1 f_r' + \dots \quad (23a)$$

$$\begin{aligned} \phi_0 = & -\frac{4\pi}{\lambda}(r - r_S) \\ & -\frac{4\pi}{\lambda}r \left( \sqrt{1 + \left( \frac{f_a + f_{dc}}{f_{aM;rS}} \right)^2} - \left( \frac{f_a + f_{dc}}{f_{aM;r}} \right)^2 - 1 \right) \end{aligned} \quad (23b)$$

$$\begin{aligned} \phi_1 = & -2\pi \frac{2(r - r_S)}{c} - 2\pi \frac{2r}{c} \\ & \times \left( 1 / \sqrt{1 + \left( \frac{f_a + f_{dc}}{f_{aM;rS}} \right)^2} - \left( \frac{f_a + f_{dc}}{f_{aM;r}} \right)^2 - 1 \right) \end{aligned} \quad (23c)$$

where  $f_{aM;rS} = 2v_{rS}/\lambda$ , and  $f_{aM;r} = 2v_r/\lambda$ . According to (23a)–(23c), after an inverse FFT (IFFT) in range, the signal can be expressed in range-Doppler domain

$$\begin{aligned} S_{\text{sub}}(\hat{t}, f_a) = & A_0 W_r(\hat{t}) W_a(f_a) \exp(j\phi_0) \\ & \times \text{sinc} \left( B \left( \hat{t} + \frac{\phi_1}{2\pi} \right) \right) \exp(-j2\pi(f_a + f_{dc})t_0) \end{aligned} \quad (24)$$

where  $B$  is the chirp bandwidth,  $\phi_0$  is the residual phase term, and  $\phi_1$  decides the range position. The first item of  $\phi_1$  is constant in a definite range, which corresponds to a straight line in range-Doppler domain. The second item of  $\phi_1$  is the residual Range cell migration term corresponding to a curve in range-Doppler domain, which should be corrected properly by an interpolation according to  $\hat{t} + (\phi_1/2\pi) = \hat{t}' - (2(r - r_S)/c)$ . In the end,  $\phi_0$  is compensated by

$$H_4(\hat{t}', f_a) = \exp(-j\phi_0). \quad (25)$$

After the interpolation and the compensation of  $\phi_0$ , the signal can be expressed as

$$\begin{aligned} S_{\text{sub}}(\hat{t}', f_a) = & A_0 W_r(\hat{t}') W_a(f_a) \\ & \times \text{sinc} \left( B \left( \hat{t}' - \frac{2(r - r_S)}{c} \right) \right) \exp(-j2\pi(f_a + f_{dc})t_0). \end{aligned} \quad (26)$$

After RCMC, azimuth focusing is in stage. BAS proposed in [7] is a high-efficiency subaperture azimuth focusing algorithm, which is used here to get the final SAR image.

### E. Computational Burden Analysis

Suppose the raw data have  $M$  range samples and  $N$  azimuth samples. The sinc interpolation kernel length is  $K$ . From the flowchart in Fig. 10, we can see that the proposed imaging algorithm contains two range FFT/IFFTs, one azimuth FFT/IFFT, four phase multiplications (H2 and H3 can be merged to one phase multiplication), three interpolations, and BAS approach;

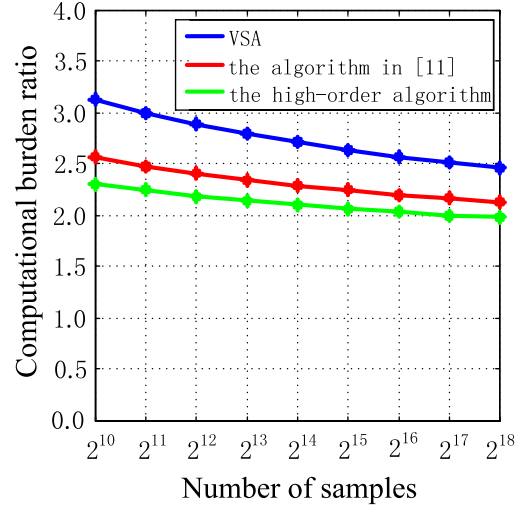


Fig. 11. Ratios of computational burdens of the three algorithms to that of CSA.

TABLE II  
SIMULATION PARAMETERS

Carrier frequency	9.65 GHz
Chirp bandwidth	1.2 GHz
Data take duration	15.5 s
Total azimuth bandwidth	61.23 kHz
PRF	40 kHz
Azimuth resolution	0.15 m
Scaling range	650.34 km
Rotation range	1625.8 km
Range scene size	10 km
Azimuth scene size	30 km
Incidence angle	34.8°
Central point (longitude/latitude)	-105°/45°
Doppler centroid variation	-15.26 kHz~15.26 kHz

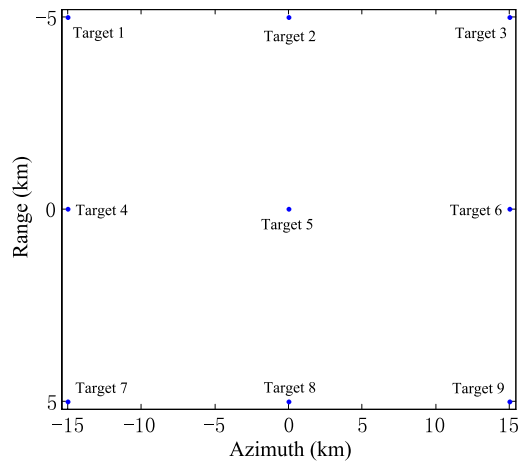


Fig. 12. Positions of nine targets.

whereas the BAS approach contains three azimuth FFT/IFFTs and three phase multiplications. Thus, the overall computational burden is

$$\begin{aligned} 2N \frac{M}{2} \log_2 M + 4M \frac{N}{2} \log_2 N + 6MN + 3KMN \\ = (\log_2 M + 2\log_2 N + 3K + 6) MN. \end{aligned} \quad (27)$$

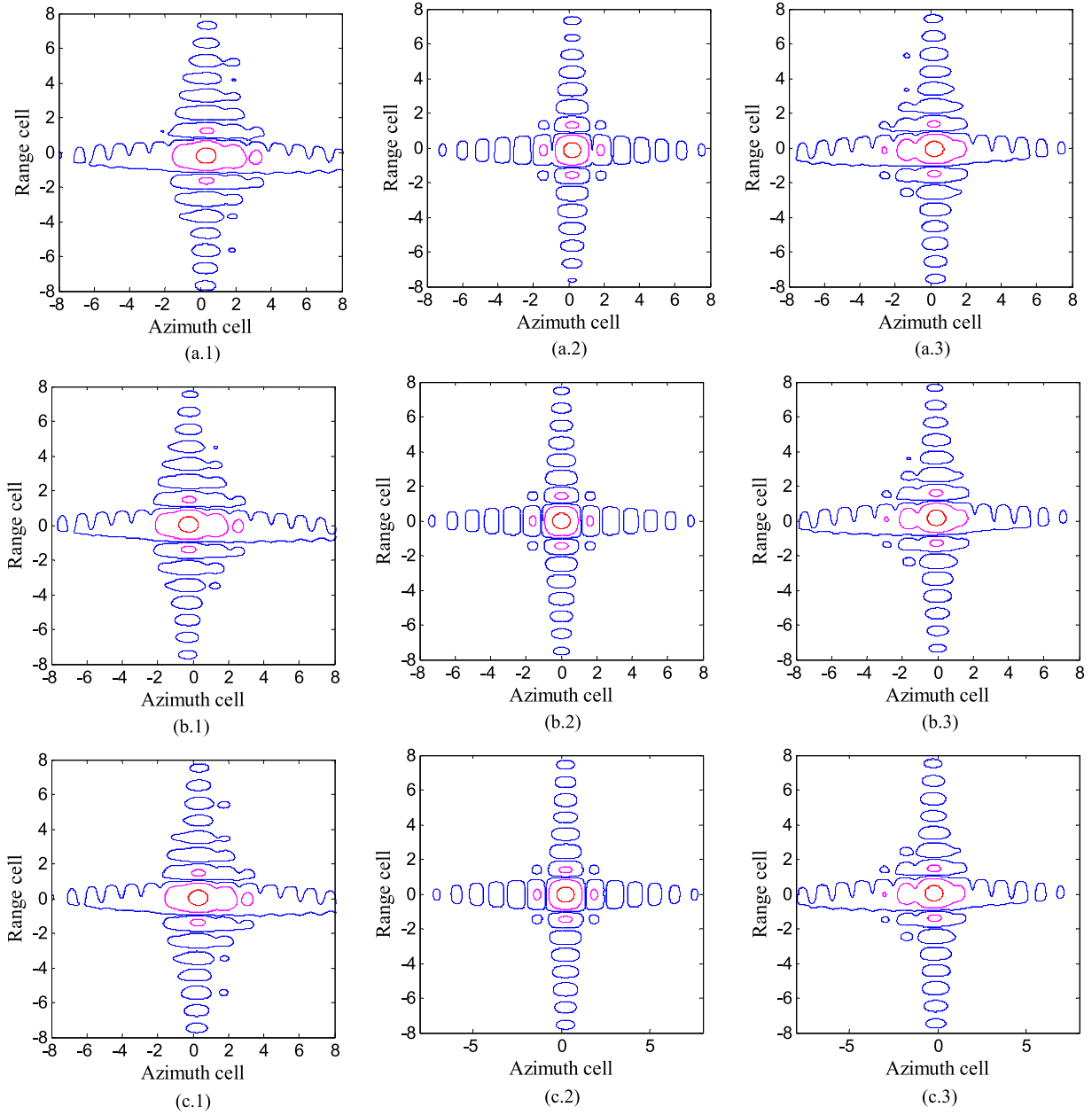


Fig. 13. Results of the algorithm proposed in [11]. (a) Results of targets 1–3. (b) Results of targets 4–6. (c) Results of targets 7–9. Contour lines at  $-3$ ,  $-15$ , and  $-30$  dB.

Usually,  $K=12$  is sufficient to provide an accurate interpolation in the case of very high resolution. Using 12-point sinc interpolation, the computational burden is  $(\log_2^M + 2\log_2^N + 42)MN$ . In the algorithm proposed in [11], suppose the azimuth processing in the last stage is realized by BAS approach. Then the computational burden is

$$2N \frac{M}{2} \log_2^M + 4M \frac{N}{2} \log_2^N + (2K + 5)MN \\ = (\log_2^M + 2\log_2^N + 2K + 5)MN \quad (28)$$

without including the stop-and-go correction and the atmospheric correction. Using 12-point sinc interpolation, the computational burden is  $(\log_2^M + 2\log_2^N + 29)MN$ . In the high-order imaging algorithm proposed in [10], there is a 2-D

correlation processing. Using a correlation window with 16 points as suggested in [10], the computational burden is

$$4N \frac{M}{2} \log_2^M + 2M \frac{N}{2} \log_2^N + 23MN \\ = (2\log_2^M + \log_2^N + 23)MN. \quad (29)$$

In the case of very high resolution, the ratio of the computational burden brought by interpolations is reduced due to the great value of  $\log_2^M$  and  $\log_2^N$ . Using the computational burden of standard Chirp scaling algorithm (CSA) [17]  $(\log_2^M + \log_2^N + 3)MN$  for reference, suppose there are  $M = N$  samples both in range and azimuth,  $K = 12$ , then the ratios of computational burdens of the three algorithms to that of CSA are plotted in Fig. 11, where the ratios are 2.71,

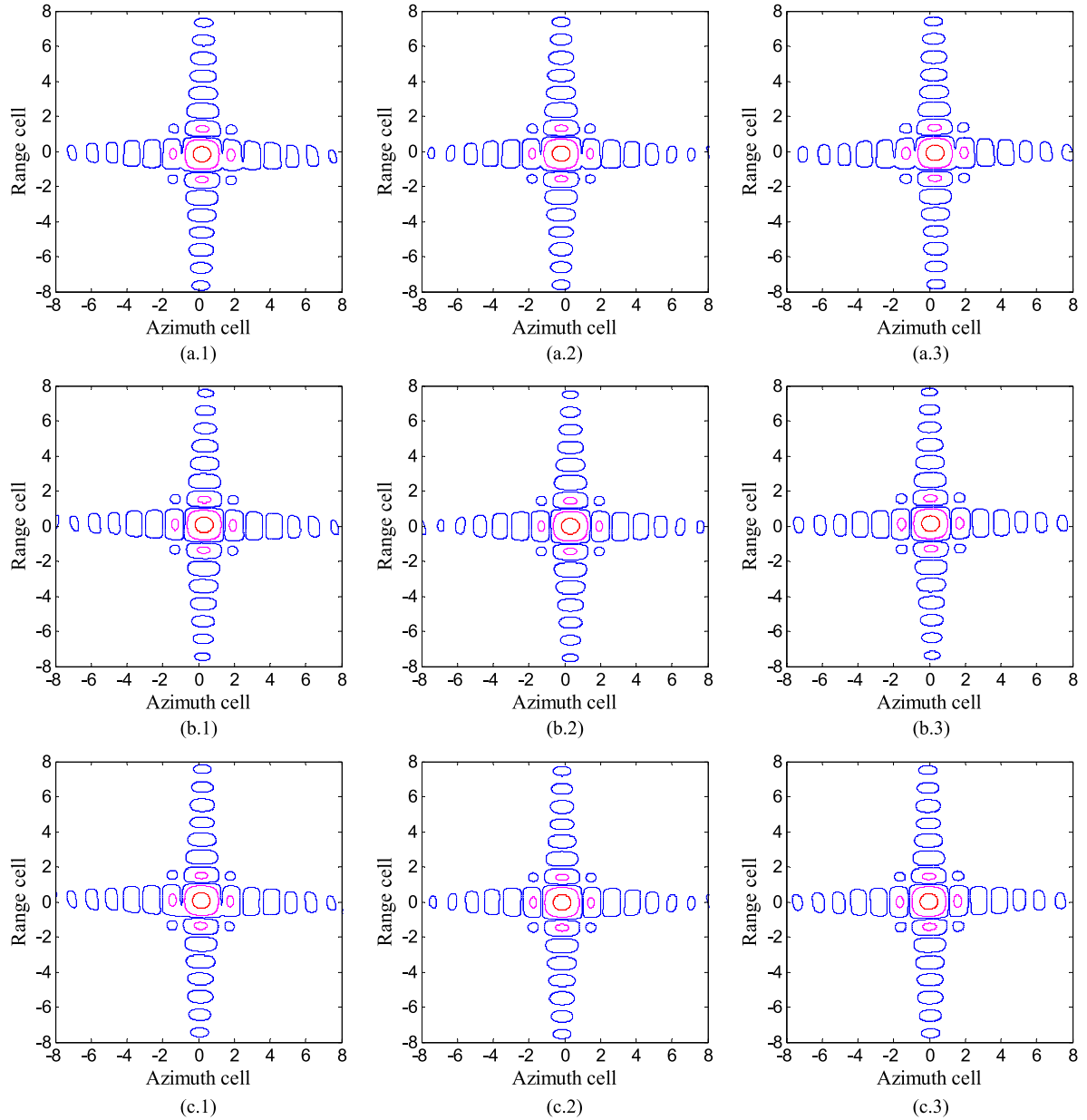


Fig. 14. Results of the proposed VSA algorithm. (a) Results of targets 1–3. (b) Results of targets 4–6. (c) Results of targets 7–9. Contour lines at  $-3$ ,  $-15$ , and  $-30$  dB.

2.29, and 2.10, respectively, when  $M = N = 2^{14} = 16384$ . Hence, we can see that the computational burden of the imaging algorithm proposed in this paper has no essential difference from those of the algorithms proposed in [10] and [11], but there is a significant increase in imaging quality. Moreover, for the interpolation in SAR imaging, there are some approaches to enhance the efficiency, such as special hardware systems designed for SAR algorithms containing interpolations [21], parallel computing [22], and so on.

#### F. Discussion

In summary, two key points of the proposed imaging algorithm are the use of accurate EARM, which meets the needs of very high resolution and large azimuth scene size space-

borne sliding spotlight SAR, and the application of velocity scaling to get azimuth invariant equivalent velocity through azimuth resampling. BAS is adopted to perform the azimuth focusing.

It should be noted that the aforementioned imaging processing does not consider the approximation error of stop-and-go model and the atmospheric effects, which were studied systematically in [11] and [23]–[27].

#### IV. SIMULATION RESULTS

Here, the simulation results are provided to validate the proposed imaging algorithm. Satellite orbit parameters are listed in Table I in Section II, and simulation parameters are listed

TABLE III  
IMAGING PERFORMANCES OF NINE TARGETS

Target	Azimuth			Range		
	$\rho_a$ (m)	PSLR(dB)	ISLR(dB)	$\rho_r$ (m)	PSLR(dB)	ISLR(dB)
1	0.169/ <b>0.150</b>	-7.01/ <b>-13.2</b>	-7.10/ <b>-10.6</b>	0.111/ <b>0.111</b>	-13.4/ <b>-13.4</b>	-9.99/ <b>-9.89</b>
2	0.150/ <b>0.151</b>	-13.5/ <b>-13.6</b>	-10.7/ <b>-10.7</b>	0.111/ <b>0.111</b>	-13.3/ <b>-13.3</b>	-9.83/ <b>-9.82</b>
3	0.157/ <b>0.150</b>	-8.82/ <b>-13.1</b>	-8.67/ <b>-10.5</b>	0.111/ <b>0.111</b>	-13.4/ <b>-13.3</b>	-9.96/ <b>-9.88</b>
4	0.166/ <b>0.150</b>	-7.31/ <b>-13.4</b>	-7.36/ <b>-10.7</b>	0.111/ <b>0.111</b>	-13.3/ <b>-13.3</b>	-9.96/ <b>-9.97</b>
5	0.150/ <b>0.150</b>	-13.6/ <b>-13.7</b>	-10.8/ <b>-10.8</b>	0.111/ <b>0.111</b>	-13.3/ <b>-13.3</b>	-9.93/ <b>-9.93</b>
6	0.156/ <b>0.150</b>	-9.08/ <b>-13.3</b>	-8.92/ <b>-10.6</b>	0.111/ <b>0.111</b>	-13.3/ <b>-13.3</b>	-9.96/ <b>-9.95</b>
7	0.167/ <b>0.149</b>	-7.19/ <b>-13.3</b>	-7.27/ <b>-10.6</b>	0.111/ <b>0.111</b>	-13.1/ <b>-13.3</b>	-9.73/ <b>-9.87</b>
8	0.149/ <b>0.149</b>	-13.6/ <b>-13.6</b>	-10.7/ <b>-10.8</b>	0.111/ <b>0.111</b>	-13.3/ <b>-13.3</b>	-9.82/ <b>-9.81</b>
9	0.155/ <b>0.149</b>	-9.07/ <b>-13.2</b>	-8.92/ <b>-10.6</b>	0.111/ <b>0.111</b>	-13.2/ <b>-13.3</b>	-9.79/ <b>-9.87</b>

in Table II. Nine targets spread out in the scene evenly, as indicated in Fig. 12.

The results of the algorithm proposed in [11] are shown in Fig. 13. It can be seen that the azimuth defocusing of targets 1, 3, 4, 6, 7, and 9 is serious due to the inaccurate MCRM model. The results of the proposed algorithm are shown in Fig. 14. It can be seen that all targets are focused well. The imaging performances of nine targets are listed in Table III, where the numbers before the slash represent the performances of the algorithm proposed in [11], and the bold numbers after the slash represent those of the proposed algorithm. The ideal range resolution is 0.111 m without windowing the range filter. The ideal azimuth resolutions of targets 1–3, 4–6, and 7–9 are 0.150, 0.149, and 0.149 m, respectively, without windowing the azimuth filter. The ideal PSLR and ISLR in range and azimuth are  $-13.3$  and  $-9.68$  dB, respectively. According to Table III, it can be observed that both algorithms have good performances in range. The algorithm proposed in [11] leads to a maximum 13% deterioration of the azimuth resolution, a maximum  $-7.01$  dB of the azimuth PSLR level, and a maximum  $-7.10$  dB of the azimuth ISLR level. It should be noted that the azimuth imaging performances here are worse than that shown in Fig. 7 in Section II-B, because the analysis in Section II-B does not consider the rotation of the radar beam in the sliding spotlight mode. It can be observed that the algorithm proposed in this paper leads to a very small deterioration of the azimuth resolution less than 1%, azimuth PSLR level under  $-13.1$  dB, and azimuth ISLR level under  $-10.5$  dB. The imaging performances have been improved significantly by the proposed method.

In the simulation of this section, the sinc interpolation kernel length is set to 12. To verify the results of the computational burden analysis given in Section III-E, the additional program of standard CSA is executed for reference. All the programs are executed in parallel. It shows that the ratios of the time costs by the algorithm proposed in [11] and VSA to that by standard CSA are 1.79 and 2.27, respectively. Hence, we can see that the time cost of the algorithm proposed in this paper has no essential difference from that of the algorithm proposed in [11], but there is a significant improvement in imaging quality.

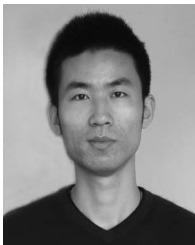
## V. CONCLUSION

In very high resolution and large azimuth scene size spaceborne sliding spotlight SAR, the hyperbolic range history is inaccurate, and the variation of the equivalent velocity in azimuth dimension cannot be ignored. For this problem, this paper proposes an EARM, which can precisely take into account the spaceborne curved orbit. Then the VSA based on this new range model is proposed with detailed procedures and block diagram. The results of the simulation validate the effectiveness of the new range model and the imaging algorithm.

## REFERENCES

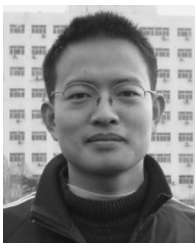
- [1] J. Mittermayer, A. Moreira, and O. Loffeld, "Spotlight SAR data processing using the frequency scaling algorithm," *IEEE Trans. Geosci. Remote Sens.*, vol. 37, no. 5, pp. 2198–2214, Sep. 1999.
- [2] G. D. Callaghan and I. D. Longstaff, "Wide-swath space-borne SAR using a quad-element array," *Proc. Inst. Elect. Eng.—Radar, Sonar Navig.*, vol. 146, no. 3, pp. 159–165, Jun. 1999.
- [3] K. Eldhuset, "Ultra high resolution spaceborne SAR processing," *IEEE Trans. Aerosp. Electron. Syst.*, vol. 40, no. 1, pp. 370–378, Jan. 2004.
- [4] G. Krieger, N. Gebert, and A. Moreira, "Multidimensional waveform encoding: A new digital beamforming technique for synthetic aperture radar remote sensing," *IEEE Trans. Geosci. Remote Sens.*, vol. 46, no. 1, pp. 31–46, Jan. 2008.
- [5] A. Meta, J. Mittermayer, P. Prats, R. Scheiber, and U. Steinbrecher, "TOPS imaging with TerraSAR-X: Mode design and performance analysis," *IEEE Trans. Geosci. Remote Sens.*, vol. 48, no. 2, pp. 759–769, Feb. 2010.
- [6] J. Mittermayer *et al.*, "Bidirectional SAR imaging mode," *IEEE Trans. Geosci. Remote Sens.*, vol. 51, no. 1, pp. 601–614, Jan. 2013.
- [7] P. Prats, R. Scheiber, J. Mittermayer, A. Meta, and A. Moreira, "Processing of sliding spotlight and TOPS SAR data using baseband azimuth scaling," *IEEE Trans. Geosci. Remote Sens.*, vol. 48, no. 2, pp. 770–780, Feb. 2010.
- [8] J. Mittermayer, R. Lord, and E. Boerner, "Sliding spotlight SAR processing for TerraSAR-X using a new formulation of the extended chirp scaling algorithm," in *Proc. IEEE IGARSS*, Toulouse, France, Jul. 21–25, 2003, vol. 3, pp. 1462–1464.
- [9] F. He, Q. Chen, Z. Dong, and Z. Y. Sun, "Processing of ultrahigh-resolution spaceborne sliding spotlight SAR data on curved orbit," *IEEE Trans. Aerosp. Electron. Syst.*, vol. 49, no. 2, pp. 819–839, Apr. 2013.
- [10] P. Wang, W. Liu, J. Chen, M. Niu, and W. Yang, "A high-order imaging algorithm for high-resolution spaceborne SAR based on a modified equivalent squint range model," *IEEE Trans. Geosci. Remote Sens.*, vol. 53, no. 3, pp. 1225–1235, Mar. 2015.
- [11] P. Prats-Iraola *et al.*, "On the processing of very high resolution spaceborne SAR data," *IEEE Trans. Geosci. Remote Sens.*, vol. 52, no. 10, pp. 6003–6016, Oct. 2014.

- [12] K. Eldhuset, "A new fourth-order processing algorithm for spaceborne SAR," *IEEE Trans. Aerosp. Electron. Syst.*, vol. 34, no. 3, pp. 824–835, Jul. 1998.
- [13] C. Cafforio, C. Prati, and F. Rocca, "SAR data focusing using seismic migration techniques," *IEEE Trans. Aerosp. Electron. Syst.*, vol. 27, no. 2, pp. 194–207, Mar. 1991.
- [14] R. Lanari, M. Tesauro, E. Sansosti, and G. Fornaro, "Spotlight SAR data focusing based on a two-step processing approach," *IEEE Trans. Geosci. Remote Sens.*, vol. 39, no. 9, pp. 1993–2004, Sep. 2001.
- [15] G. C. Sun, M. D. Xing, Y. Wang, J. Yang, and Z. Bao, "A 2-D space-variant chirp scaling algorithm based on the RCM equalization and subband synthesis to process geosynchronous SAR data," *IEEE Trans. Geosci. Remote Sens.*, vol. 52, no. 8, pp. 4868–4880, Aug. 2014.
- [16] M. Born and E. Wolf, *Principles of Optics*, 5th ed. Oxford, U.K.: IEEE, 1975.
- [17] R. K. Raney, H. Runge, R. Bamler, I. Cumming, and F. H. Wong, "Precision SAR processing using chirp scaling," *IEEE Trans. Geosci. Remote Sens.*, vol. 32, no. 4, pp. 786–799, Jul. 1994.
- [18] I. G. Cumming and F. H. Wong, *Digital Processing of Synthetic Aperture Radar Data. Algorithms and Implementation*. Boston, MA, USA: IEEE, 2005.
- [19] R. Lanari, "A new method for the compensation of the SAR range cell migration based on the chirp Z-transform," *IEEE Trans. Geosci. Remote Sens.*, vol. 33, no. 5, pp. 1296–1299, Sep. 1995.
- [20] D. D'Aria and A. Monti Guarnieri, "High-resolution spaceborne SAR focusing by SVD-Stolt," *IEEE Geosci. Remote Sens. Lett.*, vol. 4, no. 4, pp. 639–643, Oct. 2007.
- [21] Pflitzner, F. Cholewa, P. Pirsch, and H. Blume, "A flexible hardware architecture for real-time airborne wavenumber domain SAR processing," in *Proc. 9th EUSAR Conf.*, Nuremberg, Germany, Apr. 23–26, 2012, pp. 28–31.
- [22] F. Kraja, G. Acher, and A. Bode, "Parallelization techniques for the 2D Fourier matched filtering and interpolation SAR algorithm," in *Proc. IEEE Aerosp. Conf.*, Big Sky, MT, USA, Mar. 3–10, 2012, pp. 1–10.
- [23] H. Breit *et al.*, "TerraSAR-X SAR processing and products," *IEEE Trans. Geosci. Remote Sens.*, vol. 48, no. 2, pp. 727–740, Feb. 2010.
- [24] A. Ribalta, "Time-domain reconstruction algorithms for FMCW-SAR," *IEEE Geosci. Remote Sens. Lett.*, vol. 8, no. 3, pp. 396–400, May 2011.
- [25] Y. Liu *et al.*, "Echo model analyses and imaging algorithm for high-resolution SAR on high-speed platform," *IEEE Trans. Geosci. Remote Sens.*, vol. 50, no. 3, pp. 933–950, Mar. 2012.
- [26] M. Jehle, D. Perler, D. Small, A. Schubert, and E. Meier, "Estimation of atmospheric path delays in TerraSAR-X data using models vs. measurements," *Sensors*, vol. 8, no. 12, pp. 8479–8491, Dec. 2008.
- [27] M. Eineder, C. Minet, P. Steigenberger, X. Cong, and T. Fritz, "Imaging geodesy—Toward centimeter-level ranging accuracy with TerraSAR-X," *IEEE Trans. Geosci. Remote Sens.*, vol. 49, no. 2, pp. 661–671, Feb. 2011.



**Yuan Wu** was born in Hebei, China, in March 1987. He received the B.S. degree in electrical engineering from Xidian University, Xi'an, China, in 2009. He is currently working toward the Ph.D. degree in the National Laboratory of Radar Signal Processing, Xidian University.

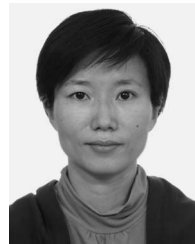
His research interests include synthetic aperture radar imaging and inverse synthetic aperture radar imaging.



**Guang-Cai Sun** (M'13) was born in Hubei, China, in December 1984. He received the B.Sc. degree in communications engineering from the Post and Telecommunications Institute, Xi'an, China, in 2006 and the Ph.D. degree in electrical engineering from Xidian University, Xi'an, in 2012.

He is currently a Researcher with the National Laboratory of Radar Signal Processing, Xidian University. He has authored or coauthored one book and over 50 papers. His research interests include imaging of several synthetic aperture radar modes

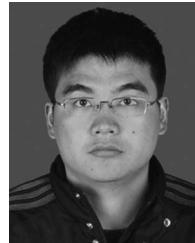
and moving target detection and imaging.



developing.

**Chun Yang** was born in Henan, China, in 1976. She received the M.S. and Ph.D. degrees in telecommunication engineering from Harbin Engineering University, Harbin, China, in 2003 and 2005, respectively.

Since 2005, she has been with the Radar Research Laboratory, Beijing Institute of Technology, Beijing, China. Since 2007, she has been with the Institute of Electronics, Chinese Academy of Sciences, Beijing. Her current research interests include traditional real aperture radar data processing and synthetic aperture radar echo simulation and imaging algorithm



**Jun Yang** was born in Hubei, China, in October 1984. He received the B.Sc. degree in computer science and technology from the Xi'an Institute of Posts and Telecommunications, Xi'an, China, in 2006. He is currently working toward the Ph.D. degree in the National Laboratory of Radar Signal Processing, Xidian University, Xi'an.

His research interests include synthetic aperture radar imaging and electronic countermeasure.



**Mengdao Xing** (M'04) was born in Zhejiang Province, China, in November 1975. He received the B.S. and Ph.D. degrees in electrical engineering from Xidian University, Xi'an, China, in 1997 and 2002, respectively.

He is currently a Full Professor with the National Laboratory of Radar Signal Processing, Xidian University. He was also with the National Key Laboratory of Microwave Imaging Technology, Institute of Electronics, Chinese Academy of Sciences, Beijing, China. He has authored or coauthored two books and

over 200 papers. His research interests include synthetic aperture radar (SAR), inversed SAR, and sparse signal processing.



**Zheng Bao** (M'80–SM'90) was born in Jiangsu, China. He received the B.S. degree in radar engineering from Xidian University, Xi'an, China, in 1953.

He is currently a Professor with Xidian University, Xi'an, China, where he is also the Chairman of the Academic Board of the National Laboratory of Radar Signal Processing. He has authored or coauthored six books and over 300 papers. His current research fields include space–time adaptive processing, radar imaging (SAR/ISAR), automatic target recognition, and over-the-horizon-radar signal

processing.